**IEEE Sensors Council**

A Numerical Analysis of Rectangular Open Channel Embedded TiO$_2$-Au-MXene Employed PCF Biosensor for Brain Tumor Diagnosis

Shivam Singh, Bhargavi Chaudhary, *Student Member, IEEE,* Rajeev Kumar, *Member, IEEE,* Anurag Upadhyay and Santosh Kumar, *Senior Member, IEEE*

Abstract— In this work, a surface plasmon resonance (SPR) plasmonic photonic crystal fiber (PCF) biosensor embedded with a rectangular open channel (ROC) is proposed, enabling precise detection and discrimination between healthy and tumorous brain tissues. Healthy and tumorous tissues are considered liquid tissues, each possessing its own distinctive refractive index (RI). The ROC is coated with gold (Au) to generate surface plasmons. To facilitate ample biomolecules, a thin Ti$_3$C$_2$Tx-MXene layer is functionalized over gold. A thin TiO$_2$ layer is coated on the ROC surface to strongly hold the Au nanoparticles, ensuring improved sensing performance. Healthy, cancerous, and tumor tissue samples exhibit unique resonance wavelengths, allowing for their diagnosis through the measurement of shifts in their respective resonance wavelengths. The essential performance parameters, including sensitivity (S), full width at half maximum (FWHM), and figure of merit (FoM) are evaluated. The computed sensitivities for normal and abnormal tissues *i.e.*, gray matter, cerebrospinal fluid and oligodendroglioma are 12352.94 nm/RIU, 2030.45 nm/RIU, and 672.26 nm/RIU, measured with respect to white matter and the wall of a solid brain. And, for tumorous tissues (cancers and tumors) such as glioblastoma, lymphoma and metastasis, the sensitivities are 800 nm/RIU, 774.9 nm/RIU, and 643.26 nm/RIU, measured with respect to low grade glioma (Benign). Additionally, the proposed biosensor's resolution (R) ranges from 1.25×10^{-4} to 8.09×10^{-6} RIU along with the maximum FoM of 126.05 RIU^{-1}. Hence, this biosensor is poised to excel in the detection of tumor and cancer tissues, making it a promising candidate for advancing medical diagnostics.
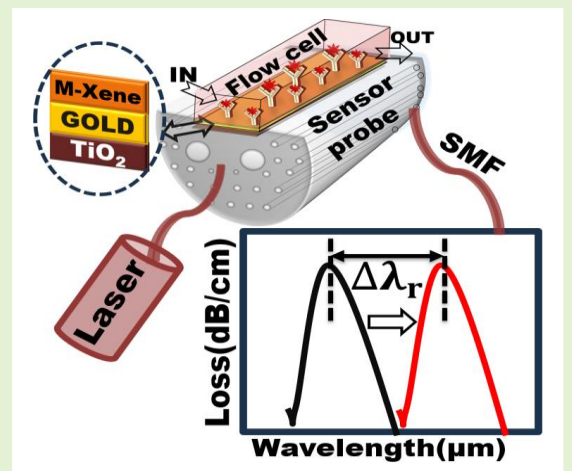
Index Terms— Optical Biosensor, surface plasmon resonance, photonic crystal fiber Ti$_3$C$_2$Tx-MXene, brain tumor

I. INTRODUCTION

OVER the last few decades, significant research efforts have been focused on the advancement of cost-effective, and reliable biosensors capable of detecting minuscule concentrations of analytes. A wide range of sensors have been innovated and produced, employing various technologies to monitor and detect cells and fluids. Photonic crystals (PhC)-based PCFs have emerged as popular choices among these technologies due to their promising features. These fibers possess an ultra-compact size, resistance to electromagnetic interference, require minimal analyte quantities, offer flexibility in structural design, and enable seamless integration into various systems [1], [2]. In recent years, the fusion of the SPR phenomenon with PCF has emerged as a highly effective and prominent sensing technology [3]. SPR employed PCF biosensors hold the potential to transform diverse domains, especially in biomedical studies [4]–[6]. PCF biosensors offer high sensitivity for detecting biomolecules and analytes. The interaction of the evanescent field with the analyte on the surface of the PCF allows for precise measurements of RI changes. This sensitivity enables the detection of extremely low concentrations of analytes, making these sensors valuable for

Corresponding author: Bhargavi Chaudhary; Santosh Kumar
Shivam Singh is with Department of ECE, ABES Engineering College Ghaziabad, Uttar Pradesh 201009, India (e-mail:shivams20@gmail.com)
Bhargavi Chaudhary is with Department of EE, Indian Institute of Technology Delhi, New Delhi 110016, India (e-mail-bhargavichy31@yahoo.com)
Rajeev Kumar is with Department of ECE,Graphic Era(Deemed to be University) Dehradun, Uttarakhand 248002, India (e-mail:rajeevkrc@gmail.com)

Anurag Upadhyay is with Department of ASH, Rajkiya Engineering College Azamgarh, Uttar Pradesh 276201, India (e-mail:anurag.upadhyay009@gmail.com)
Santosh Kumar is with the Department of Electronics and Communication Engineering, Koneru Lakshmaiah Education Foundation, Vaddeswaram, Andhra Pradesh – 522302, India (e-mail: santosh@kluniversity.in)

medical diagnostics. Over the years, there have been significant advancements in SPR-based PCF sensors, employing a variety of plasmonic materials and geometries. Among these sensor types, single-sided flat (D-shaped) PCF sensors have captured the attention of researchers. This interest stems from their enhanced fabrication feasibility and simplified process of depositing a metal layer on the external flat area [7]. In the realm of biosensing, scientists have delved into the exploration and utilization of the unique optical characteristics exhibited by two-dimensional (2D) nanomaterials such graphene, and MoS_2. to improve the sensor's performance in detecting biological substances. However, these materials encounter certain limitations, including inadequate biocompatibility and significant hydrophobicity. To address these issues, researchers have turned their attention to MXene, which presents a promising solution. In recent years, MXene materials have gained considerable traction among the scientific community due to their advantageous optical properties, opening up new avenues for biosensing applications. MXene, part of the transition-metal carbide or nitride family, exhibits metallic behavior due to a high density of states at the Fermi level. Ti_3C_2Tx is the most extensively researched MXene material, offering versatile surface functional groups for property adjustments and excellent compatibility with other materials. This high-performance MXene can form hybrid films with traditional plasma metals, enhancing surface EM field intensity and promoting surface plasmon excitation for increased sensitivity. Hence, the presence of MXene as a thin layer on the sensor surface enhances the interaction between the analyte molecules and the plasmonic field, leading to improved signal transduction and detection sensitivity [8], [9]. Based on the merits of SPR-based PCF sensors for biomedical applications described above, a variety of biomedical sensors, including those for cancer cell, hemoglobin, protein, and malaria detection, have been developed and validated [10]–[13]. However, within the realm of PCF biomedical applications, limited literatures focuses on discrepating between healthy and diseased brain tissues. Additionally, a lack of research has also been noted in studies that develop, test, and create sensors with appealing sensing capabilities. Addressing these gaps in research could lead to important developments in the field of brain tissue analysis and improve the diagnosis of the brain-related disorders.

Brain and other nervous system cancer ranks as the 10th most common cause of death for both men and women. As per the annual report for 2021 from the United States (US) Central Brain Tumor Registry, brain tumors have been observed in individuals across all age groups, races, ethnicities, and genders [14]. Approximately, 85% to 90% of primary central nervous system (CNS) tumors are attributed to brain tumors. In 2020, an estimated 308,102 individuals were diagnosed with primary brain tumors, resulting in 251,329 global fatalities from cancerous brain and CNS tumors. Studies have indicated a higher incidence of malignant brain tumors in males, whereas non-malignant tumor cases tend to be more prevalent in females [15], [16]. Additionally, it is noteworthy that malignant brain tumors constitute approximately 33% of all reported cases among brain and other CNS tumors. It is projected that in 2023, there will be approximately 24,810 cases of primary cancerous brain and CNS tumors diagnosed in the United States alone.

[17]. These statistics highlight the life-threatening nature of unhealthy or diseased brain tissues, particularly those that are cancerous. Therefore, it is crucial to seriously invest efforts in designing, testing, and potentially manufacturing various devices, sensors, and machines aimed at addressing such impairments in medical practice. By doing so, we can improve the prognosis and treatment outcomes for individuals affected by these conditions. Despite a limited number of studies exploring tumor detection, particularly through the use of 1D-PhCs, there is a notable scarcity in the field when it comes to sensing and distinguishing between different types of brain tumors and cancerous tissues. In 2020, W.M. Nouman et al. [18] introduced a brain cancer sensor incorporating a defective 1D-PhC design. However, the limitations of such structures hinder the realization of this sensor in real-time applications. One significant drawback is that 1D-PhC-based designs are typically employed as perfect mirrors and encounter issues with angular resolution. Additionally, while functionalization is feasible in 1D-PhCs, their specific design may not offer the same level of flexibility in optimizing surface interactions with biological molecules. In contrast, PCFs can be engineered to be biocompatible and easily functionalized with biomolecules or coatings, providing enhanced flexibility for optimizing surface interactions and improving specificity and selectivity for target analytes.

The primary aim of this work is to assess the proposed biosensor's efficacy in detecting brain tumors. To achieve this, we utilize a SPR-based PCF sensor probe specifically designed for the detection of various types of brain tumors. Through simulations and analysis, we have investigated the performance of the probe. The novelties in our proposed work encompass three major aspects:

(i) The designed PCF integrates a gold coated micro-rectangular channel, reducing the distance between the fiber's core and the sensing medium. This design not only enhances light coupling but also ensures secure retention of bio analytes within the rectangular channel.

(ii) The PCF design necessitates less plasmonic material, as metal deposition is confined to the ROC region exclusively.

(iii) Our contribution highlights the potential of MXene for bio analyte attachment, suggesting its promising application in SPR-based PCF biosensors tailored for detecting brain tumors. Additionally, the feasibility of fabricating the PCF biosensor using current technology is also discussed.

II. PCF BIOSENSOR COMPOSITIONS

A. Geometrical description and metal deposition

In Fig. 1(a), the proposed sensor is illustrated with a cross-sectional view highlighting its distinctive single-sided etched structure attained by utilizing a rhombus configuration of air-holes. The two large air holes close to the solid core have a diameter (D) of 2.35 µm whereas the four small air holes placed vertically on the fiber core have a diameter (d_1) 1.15 µm. The medium air holes (d_2) decorated in a hexagonal manner are measured at 1.35 µm in diameter, followed by a pitch distance (Λ) of 2.15 µm. The choice of hexagonal-patterned air holes in the cladding region is deliberate as this pattern of cladding efficiently restricts additional light scattering within the fiber core [19]. To ensure an effective mode coupling, a rectangular

open channel is embedded on the upper flat surface. The measured rectangular width (W) and the vertical elevation (R_h) from the center of core to the rectangular channel are 3.5 µm and 2.55 µm. To induce surface plasmons, a plasmonic material gold is coated on the selected rectangular opening. Further, MXene is coated over gold for strong attachment of sample's biomolecules. Further, the proposed layout for the experimental realization of the biosensor is shown in Fig.2(b).
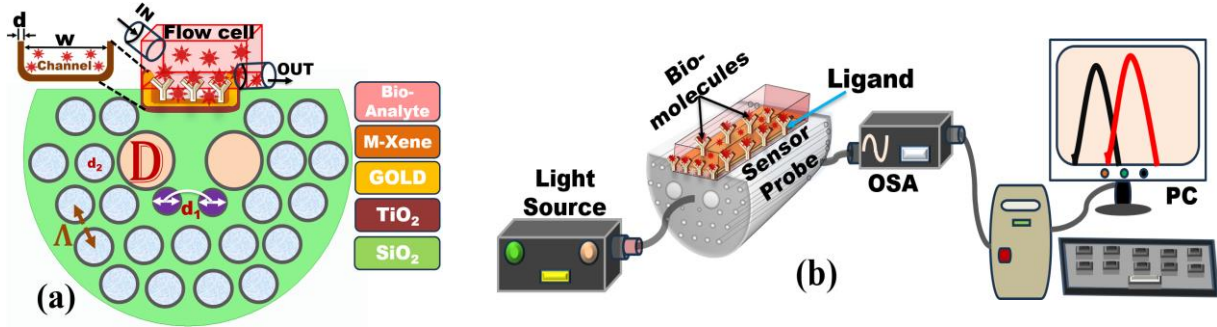

Fig. 1 (a) 2D front view and, (b) experimental layout for the proposed biosensor aimed at detecting tumor and cancer tissues

B. Material Refractive Indices

The fabrication of the suggested biosensor comprises silicon dioxide (SiO_2), titanium dioxide (TiO_2), gold (Au) and Ti_3C_2Tx -MXene as its constituent materials. SiO_2 is used as substrate material whose wavelength-dependant RI is governed by Sellmeier equation, given as follows [20].

$$n_{sio_2}^2(\lambda) = 1 + \frac{U_1\lambda^2}{\lambda^2 - V_1^2} + \frac{U_2\lambda^2}{\lambda^2 - V_2^2} + \frac{U_3\lambda^2}{\lambda^2 - V_3^2} \quad (1)$$

The weightage of coefficients U_1, U_2, U_3, V_1, V_2 and V_3 are depicted in Table I.

The RI of an adhesive material TiO_2 is expressed as [21]:

$$n_{TiO_2}^2 = 5.91 + \frac{2.441 \times 10^7}{\lambda^2 - 0.803 \times 10^7} \quad (2)$$

The selected region (rectangular) of substrate is coated with gold whose frequency dependant dielectric constant (ε_G) is governed by the Drude-Lorentz model, expressed as follows [22].

$$\varepsilon_G = \varepsilon_\infty - \frac{\omega_D^2}{\omega(\omega + j\gamma_D)} - \frac{\Delta\varepsilon\Omega_L^2}{(\omega^2 - \Omega_L^2) + J\Gamma_L\omega} \quad (3)$$

The Drude-Lorentz parameters such as frequency spectrum width (Γ_L), oscillator strength (Ω_L), plasma frequency (ω_D), damping frequency (γ_D), angular frequency (ω), high frequency permittivity(ε_∞) and the weighted coefficient ($\Delta\varepsilon$) are shown in Table II. Moreover, the RI of Ti_3C_2Tx -MXene, which depends on wavelength can be acquired using [23].

TABLE I
SALLEMEIER COEFFICIENTS FOR SIO_2

U_1	U_2	U_3	V_1(µm)	V_2(µm)	V_3(µm)
0.696 1633	0.40794 26	0.897 4794	0.06840 43	0.11624 14	9.896161

TABLE II
DRUDE- LORENTZ PARAMETERS VALUES

$\Gamma_L/2\pi$ (THz)	$\Omega_L/2\pi$ (THz)	$\omega_D/2\pi$ (THz)	$\gamma_D/2\pi$ (THz)	$\Delta\varepsilon$	ε_∞
104.86	650.07	2113.6	15.92	1.09	5.9673

TABLE III
CATEGORIZATION OF DIFFERENT BRAIN TISSUES WITH THEIR RIS

Brain tissue type	Tissue sub-category	RI	Ref.
Healthy	White matter	1.4121	[28]
	Cerebrospinal fluid	1.3333	
	Gray matter	1.3951	
Unhealthy	Wall of solid brain	1.3412	
	Oligodendroglioma	1.3531	
Tumors & Cancers	Low grade glioma (Benign)	1.432	
	Lymphoma	1.4591	
	Glioblastoma	1.447	
	Metastasis	1.4833	

C. Feasibility of Fabricating the Proposed PCF Sensor

The feasibility of fabricating a PCF pertains to the practical viability of producing a specific fiber structure. Therefore, in Fig. 2(a-c), the fabrication steps for the proposed fiber sensor are manifested. As illustrated in Fig. 2(a), the process of crafting a pre-fabricated PCF rod necessitates the use of separate silica capillaries (thick and thin) in conjunction with a solid silica rod. To build-up a piled-up circular PCF structure, the stack and draw technique is used that involves layering thin and thick capillaries along with solid rods [24]. After stacking is done, the circular PCF can be partially etched from the upper side and converted into a D-shaped PCF. A rectangular open channel can be framed on the upper flat region of the fiber using femtosecond laser or focused ion beam milling [25]. Then, the micro-ROC can be coated with gold using one of the available techniques, i.e., ALD or CVD [26]. The process of preparing MXene from the MAX phase (Ti_3AlC_2) typically involves selective etching of aluminum (Al) from the MAX phase precursor. The common etchants used for this purpose include hydrofluoric acid or a mixture of lithium fluoride (LiF) and hydrochloric acid. Subsequently, the liquid phase exfoliation or delamination technique can be used to yield a monolayer of Ti_3C_2Tx -Mxene, as shown in Fig. 2(b). Finally, the Ti_3C_2Tx -MXene can be coated onto a gold substrate[27], [28].
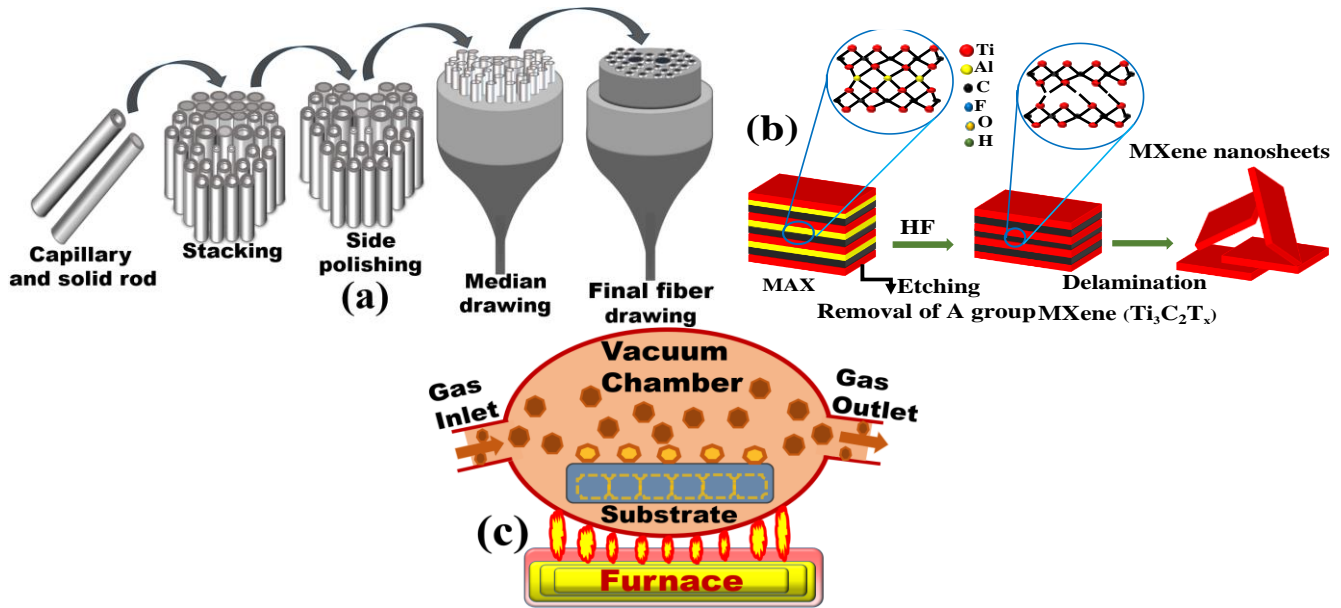
Fig. 2. The sequential fabrication steps for the proposed biosensor (a) assembling rods and capillaries in layers, culminating in the final arrangement, (b) preparation of Mxene-Ti_3C_2Tx nanosheets, and (c) employing the CVD technique for gold and Ti_3C_2Tx deposition.

D. Performance Metrics for the Biosensor

The numerical evaluation of the proposed sensor's performance is done in terms of the following parameters with the help of the standard SPR characteristics curve [20]–[22].

The modal confinement loss (ξ_{CF}) is of utmost importance in the SPR biosensor's performance evaluation, and it can be mathematically expressed as follows:

$$\xi_{CF}(dB/cm) = 8.686 \times 2\pi/\lambda \times Imag(n_{eff}) \times 10^4 \qquad (4)$$

where, $Imag(n_{eff})$ holds the imaginary fraction of the effective RI

The wavelength sensitivity (S_W) is quantified as the ratio between the shift in resonance wavelength and the shift in sensing medium RI observed in the SPR characteristic curves after biomolecule adsorption. This metric plays a crucial role as it serves as a significant indicator of the sensor's sensing capability.

$$S_W(nm/RIU) = \Delta\lambda_r/\Delta n_a \qquad (5)$$

where, $\Delta\lambda_r$ and Δn_a notify the necessary shift between the resonannt peak and the change in RI of the bio-analyte.

To assess the sensor's minimum detection capability with respect to the changes in the analyte RI, the sensor resolution (R_s) can be figured out using the following expression.

$$R_S(RIU) = \Delta\lambda_{min} \times \Delta n_a/\lambda_r \qquad (6)$$

Here, $\Delta\lambda_{min}$, the minimal resolution is assumed to be 0.1nm.

The Figure of Merit (FoM) is a quantitative parameter used to evaluate the sensor's performance. It provides a single metric that combines several relevant performance parameters, such as sensitivity and resolution.

$$FoM(RIU^{-1}) = S_W/FWHM \qquad (7)$$

Here, FWHM stands for full width at half maximum (i.e., $\lambda_{0.5}$) of the characteristic curve.

III. MODES OF OPERATION, RESULTS, AND DISCUSSION

The suggested PCF biosensor relies on the SPR phenomenon for its operation which describes the transmitted optical light confinement in two distinct regions: the core region, known as the core mode and the region at the interface between the MXene layer and the sensing medium, referred to as the surface plasmon polariton (SPP) mode. When the SPP-mode and core-mode synchronize in phase within defined transmission conditions, the SPP-mode merges with the core-mode, resulting in the emergence of SPR. Essentially, this entails that energy from the core-mode efficiently shifts to the SPP-mode. As a result, this energy transfer leads the confinement loss of the core mode to peak at the resonance wavelength (λ_r).
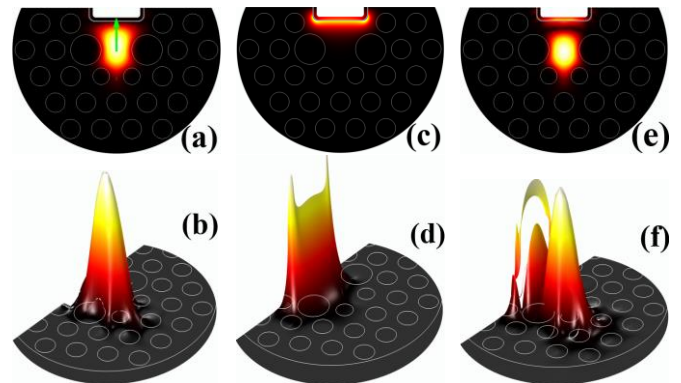

Fig. 3. Dispensation of electric filed for low grade glioma sample (n_a=1.432) in three distinct modes: core mode, SPP mode and coupling mode at $\lambda_r = 1.44$ μm.

Fig. 3 illustrates a simulated SPR biosensor representing the electric field dispensation (2D and 3D), with an arrow (green colored) indicating its polarisation state. Figs. 3(a)-(d) illustrate the y-polarized field dispensation. The visuals highlight that during core-mode propagation, the field intensity significantly surpasses that of the SPP-mode, whereas during SPP-mode propagation, the field intensity exceeds that of the core-mode.

This contrast arises because in core propagation mode, most of the transmitted optical energy is concentrated within the core region, with relatively less energy residing in the region between metal and dielectric. Conversely, in SPP propagation mode, nearly all the transmitted energy is confined within the vicinity of the metal-dielectric interface region, rather than in the core region. Specifically, Figs. 3(e)-(f) portrays the resonance mode, where the phase of core mode and SPP-mode synchronize at a resonance wavelength of 1.44 μm. Moreover, a deeper comprehension of electric field dispensation and mode-coupling in SPR biosensors can be attained through an examination of coupled-mode theory which can be formulated as follows [20]:

$$dE_1/d_z = j\gamma_1 E_1 + jkE_2 \qquad (8)$$
$$dE_2/d_z = j\gamma_2 E_2 + jkE_1 \qquad (9)$$

Here, E_1, E_2 are mode fields and γ_1, γ_2 are propagation constants associated with core mode and SPP mode. The symbols z and k are used to represent propagation length and coupling strength. Under SPR, the real fractions of γ_1 and γ_2 become equal, leading to the coupling of the core-mode with the SPP-mode. Now, if we denote β as the overall propagation constant following SPR, it can be formulated using Eq. 8 and 9, as illustrated below:

$$\gamma_\pm = \gamma_{\text{avg}} \pm \sqrt{\delta^2 + k^2} \qquad (10)$$

Here, $\gamma_{\text{avg}} = \gamma_1 + \gamma_2/2$ and $\delta = \delta_r + j\delta_j = \gamma_1 - \gamma_2/2$. Upon meeting the phase matching i.e., $\delta_r = 0$, and when δ_j is less than k, the imaginary fractions of γ_+ and γ_- become indistinguishable, yet their real fractions remain distinct. This situation results in complete coupling. Conversely, incomplete coupling takes place when the imaginary fractions of γ_+ and γ_- differ, while their real fractions remain identical.
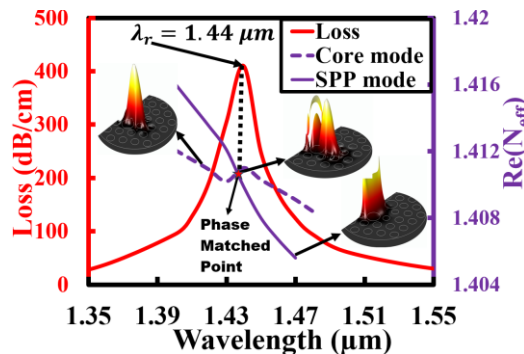

Fig. 4. Mode coupling loss and dispersion relations for a low grade glioma sample in core, SPP and coupling mode at $\lambda_r = 1.44$ μm.

In Fig. 4, the dispersion relation and mode coupling loss curve for a tumor sample of low-grade glioma are illustrated. This plot reveals an interesting feature: the real fraction of the effective refractive index Re(n_{eff}) for both the core-mode and SPP-mode converges at $\lambda_r = 1.44$ μm, which is commonly referred to as the phase-matched point. This convergence signifies that the energy associated with the core-mode becomes coupled with the SPP-mode. Consequently, the confinement loss of the core-mode reaches its maximum value (409.37dB/cm), resulting in the observation of a distinct loss peak. This phenomenon can also be justified by examining the mode-field distribution of both the core mode and SPP-mode, which is depicted in Fig. 5. Notably, at the phase matching

point, there is a significant transfer of modal energies, highlighting the pronounced mode coupling effect.

Fig. 5(a)-(d) illustrate how the effective RI's real part and confinement loss varies across various brain tissue samples: normal, abnormal, tumorous, and cancerous. This illustration highlights distinct peaks of confinement loss for each sample. These peaks occur at resonance wavelengths where the real fraction of effective RI of the core guided mode aligns with that of the SPP mode. Consequently, the distinctive loss peaks serve as a distinguishing factor, enabling the differentiation of various brain tissue samples. Figs. 5(a)-(b) display variation in confinement loss of core guided mode for brain's normal tissue samples such as white matter, gray matter, and cerebrospinal fluid. The loss peak differs for each sample.
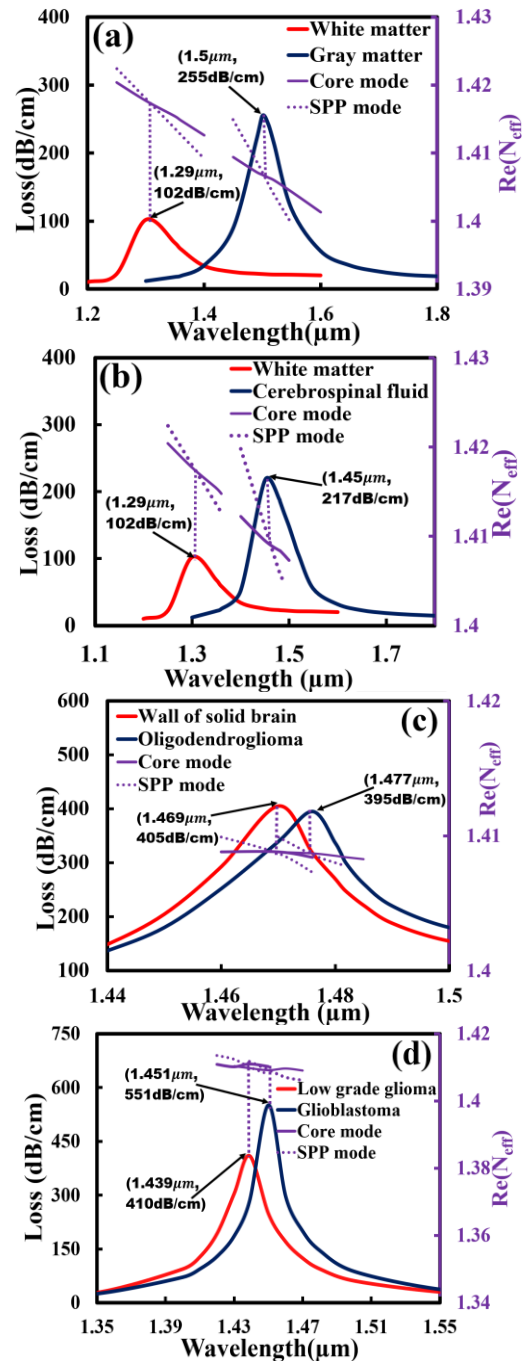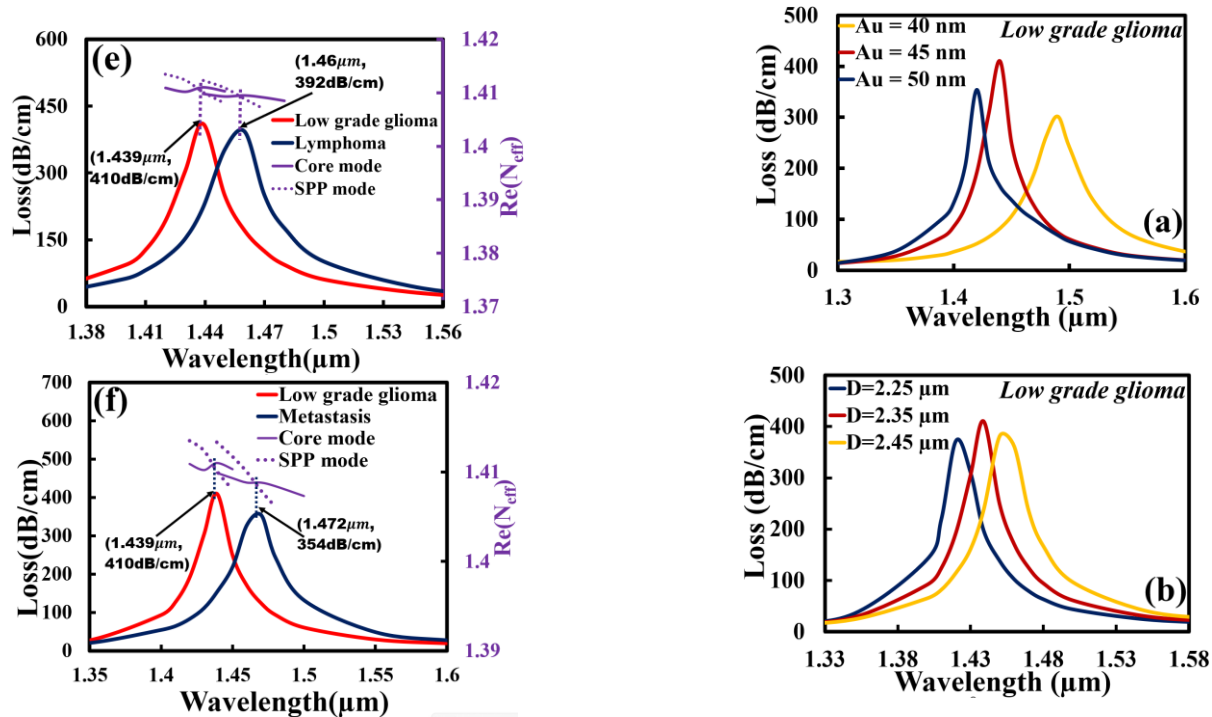
Fig. 5. Variation in effective RI's real part and confinement loss with wavelength for (a) white & gray matter (b) cerebrospinal fluid & white matter (c) the wall of solid brain & oligodendroglioma (d) low-grade glioma & glioblastoma (e) lymphoma & low-grade glioma (f) low-grade glioma & metastasis

As depicted in Fig. 5(a), the acquired resonant peaks occur at λ_r = 1.29 μm and 1.5 μm, with their corresponding peak loss values of 102 dB/cm and 255 dB/cm, respectively, for white matter (RI=1.4121) and gray matter (RI=1.3951). As a result, the shift in the resonant peak is 210 nm, enabling the maximum sensitivity (S_W) of 12,352.94 nm/RIU. Whereas the resonant peak associated with the cerebrospinal fluid sample (RI=1.3333) yields the maximum loss value of 217 dB/cm, as shown in Fig. 5(b). Fig. 5(c) reveals the confinement loss characteristics in relation to abnormal brain tissue samples, specifically the wall of the solid brain and oligodendroglioma. In this illustration, the guided mode loss peaks correspond to the solid brain wall (RI=1.3412) and oligodendroglioma (RI=1.3531) are identified at resonance wavelengths of 1.469 μm and 1.477 μm, respectively, resulting in a maximum relative sensitivity of 672.26 nm/RIU. Additionally, the effective RI and mode loss coupling characteristics for tumorous and cancer samples such as low grade glioma (Benign), glioblastoma, lymphoma, and metastasis are shown in Figs. 5(d)-(f). Fig. 5(d) reveals that the resonant peak for the low-grade glioma sample (RI=1.432) appears at λ_r = 1.439 μm with a maximum peak loss value of 410 dB/cm. Upon replacement by a glioblastoma (RI=1.447) sample, the resonant peak shifts and stabilizes at λ_r = 1.451μm, resulting in a sensitivity of 800 nm/RIU, a significant enough change to differentiate between these sample types. Furthermore, in Fig. 5 (e)-(f), the observed absorption peaks for lymphoma (RI=1.4591) and metastasis (RI=1.4833) samples compared to the low grade glioma sample are positioned at 1.46 μm and 1.472 μm, respectively. This positioning results in calculated relative sensitivities of 774.9 nm/RIU and 643.27 nm/RIU, respectively.
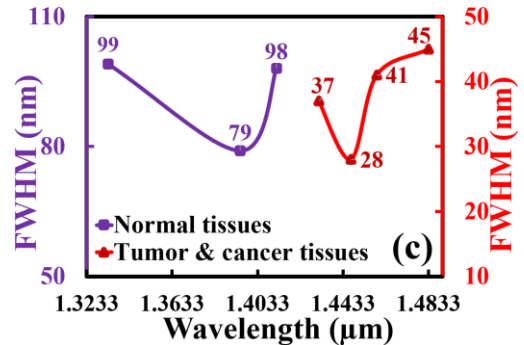

Fig. 6. Variation in resonant peak with (a) Au thickness, (b) the largest airhole diameter, and (c) FWHM variation with bio-analyte.

The structural features of the proposed biosensor, notably the variation in Au layer thickness and the the largest air hole diameter, influence the location of the resonant peak. This influence has implications for the sensor's overall performance. In Fig. 6(a), the variation in the resonant peak concerning different thicknesses the gold is depicted. The measured peak loss values for Au layer thicknesses of 40 nm, 45 nm, and 50 nm are 301.6 dB/cm, 410 dB/cm, and 354 dB/cm, respectively. The resonant peak is affected when the diameter of the biggest air hole is changed from D = 2.25 μm to 2.45 μm, as seen in Fig. 6(b). There is a discernible shift in λ_r when the largest airhole diameter is changed. Additionally, the guided mode loss also increases with increase in diameter. This happens because the closer placement of these larger air holes helps in concentrating a significant amount of light energy in the proximity of core region. This concentrated energy further facilitates strong coupling with the interface (metal-dielectric), leading to higher coupling losses. The peak loss values are 372 dB/cm, 410 dB/cm, and 382dB/cm for D = 2.25 μm, 2.35 μm, and 2.45 μm, respectively. Therefore, D = 2.35 μm is selected as the optimal size for the largest air holes. Fig. 6(c) demonstrates the FWHM values and their respective curves concerning the RI variations observed in normal, tumorous and

This article has been accepted for publication in IEEE Sensors Journal. This is the author's version which has not been fully edited and content may change prior to final publication. Citation information: DOI 10.1109/JSEN.2024.3386395

8

cancerous tissue samples. Among these, gray matter, representing normal tissue, exhibits the minimum FWHM value of 79 nm. Conversely, glioblastoma, a form of cancerous tissue, showcases a reduced FWHM value of 28 nm. These

significantly low FWHM measurements contribute to a narrow width in the confinement loss curve, thereby improving the detection accuracy of the specific bio-analyte.

TABLE IV
PERFORMANCE ASSESSMENT OF THE PROPOSED BIOSENSOR FOR VARIOUS TUMOROUS AND CANCEROUS TISSUES

Bio-analyte		RI	λ_r (nm)	S_W (nm/RIU)	FWHM (nm)	FoM (RIU^{-1})
Normal tissues	White matter	1.4121	1290	12,352.94	98	126.05
	Gray matter	1.3951	1500		79	
	White matter	1.4121	1290	2030.45	98	20.71
	Cerebrospinal fluid	1.3333	1450		99	
Abnormal tissues	Wall of solid brain	1.3412	1469	672.26	39	17.23
	Oligodendroglioma	1.3531	1477		41	
Tumors & cancers	Low grade glioma (Benign)	1.432	1439	800	37	21.62
	Glioblastoma	1.447	1451		28	
	Low grade glioma (Benign)	1.432	1439	774.90	37	20.94
	Lymphoma	1.4591	1460		41	
	Low grade glioma (Benign)	1.432	1439	643.27	37	17.38
	Metastasis	1.4833	1472		45	

Table IV provides an overview of the assessed performance metrics for the proposed biosensor. Notably, higher sensitivities are observed for the gray matter sample from normal tissue, measuring at 12,352.94 nm/RIU, and for the low-grade glioma

sample from tumorous tissue, measuring at 800 nm/RIU. Furthermore, Table IV also specifies FWHM and FoM for all considered bio analytes.

TABLE V
COMPARATIVE ASSESSMENT OF THE PROPOSED SENSOR FOR VARIOUS TUMOROUS AND CANCEROUS TISSUES

Refs.	Structure type	Tissue type	Tissue category	Sensitivity (nm/RIU)	FoM (RIU^{-1})
[12]	Bi-core PCF	Cancerous	Basal	4500	NA
			HeLa	5416	NA
[29]	2D Photonic crystal	Normal	Gray matter	1196	NA
			Cerebrospinal fluid	1332	NA
		Abnormal	Wall of solid brain	1311	NA
			Oligodendroglioma	1282	NA
		Tumorous & Cancerous	Glioblastoma	1116	NA
			Lymphoma	1100	NA
			Metastasis	1074	NA
[30]	2D Photonic crystal	Normal	Gray matter	571.4	NA
			Cerebrospinal fluid	NA	NA
		Abnormal	Wall of solid brain	1012.6	NA
			Oligodendroglioma	849	NA
		Tumorous & Cancerous	Low grade glioma	653.2	NA
			Lymphoma	578.3	NA
			Metastasis	1033	NA
This work	D-shaped PCF	Normal	Gray matter	12352.94	126.05
			Cerebrospinal fluid	2030.45	20.71
		Abnormal	Oligodendroglioma	672.26	17.23
		Tumorous & Cancerous	Low grade glioma	800	21.62
			Lymphoma	774.9	20.94
			Metastasis	643.27	17.28

The sensing performance comparison, focusing on sensitivity and FoM, between the proposed biosensor and the most recent state-of-the-art work on brain tumor diagnosis is demonstrated in Table V. It is noteworthy that the proposed biosensor exhibits

impressive performance across a range of examined brain tissue samples.

IV. CONCLUSION

A plasmonic PCF biosensor is proposed to discriminate between normal, abnormal, tumorous, and cancerous tissues. The considered normal and abnormal tissues are white matter, gray matter, and cerebrospinal fluid while the tumorous and cancerous tissues are low grade glioma, glioblastoma, lymphoma, and metastasis. Moreover, the sensor's design simplicity requires minimal gold coating, making it economical. The detection mechanism is based on refractometric sensing since each tissue sample possess a unique RI value, as shown in Table III. However, ensuring the biosensor's biocompatibility when interfacing with biological tissues or fluids is crucial, as any adverse effects could impact its clinical utility.The FEM is utilized for the assessment of dispersion characteristics, enabling the acquisition of confinement loss spectra that exhibit wavelength-dependent variations for various bio-analytes. The normal, tumorous, and cancerous tissue samples are identified by monitoring the resonance wavelengths due to their different RI values. By measuring the shift between their resonance wavelength, the wavelength sensitivity has been calculated. The biosensor under consideration demonstrates remarkable characteristics, including the maximum sensitivity of 12,352.94 nm/RIU, an exceptionally high FoM of 126.05 RIU^{-1}, and an impressively high resolution of 8.09×10^{-6} RIU. These substantial numerical outcomes position the proposed biosensor as a fitting option for applications in biological sensing. Additionally, the possible avenues for future research are to explore integrating multiple detection modalities to enhance specificity and overall accuracy in brain tumor detection and surface modifications to improve the biosensor's sensitivity.

REFERENCES

[1] Y. Zhang, Y. Zhao, and R. Lv, "A review for optical sensors based on photonic crystal cavities," *Sensors Actuators A Phys.*, vol. 233, pp. 374–389, 2015.

[2] N. A. Mohammed, O. E. Khedr, E.-S. M. El-Rabaie, and A. A. M. Khalaf, "Literature review: on-chip photonic crystals and photonic crystal fiber for biosensing and some novel trends," *IEEE Access*, vol. 10, pp. 47419–47436, 2022.

[3] A. K. Agrawal, A. Suchitta, and A. Dhawan, "Enhanced SPR-based localized and bulk sensing using a plasmonic nanopillar array with spacer," *IEEE Sens. J.*, vol. 22, no. 7, pp. 6491–6508, 2021.

[4] X. Kong et al., "Chemical and biological sensing using diatom photonic crystal biosilica with in-situ growth plasmonic nanoparticles," *IEEE Trans. Nanobioscience*, vol. 15, no. 8, pp. 828–834, 2016.

[5] G. Li, R. Singh, J. Guo, B. Zhang, and S. Kumar, "Nb2CTx MXene-assisted double S-tapered fiber-based LSPR sensor with improved features for tyramine detection," *Appl. Phys. Lett.*, vol. 122, no. 8, 2023.

[6] J. Chen et al., "CRISPR-powered optothermal nanotweezers: Diverse bio-nanoparticle manipulation and single nucleotide identification," *Light Sci. Appl.*, vol. 12, no. 1, p. 273, 2023, doi: 10.1038/s41377-023-01326-9.

[7] X. Chen, L. Xia, and C. Li, "Surface plasmon resonance sensor based on a novel D-shaped photonic crystal fiber for low refractive index detection," *IEEE Photonics J.*, vol. 10, no. 1, pp. 1–9, 2018.

[8] R. Singh, W. Zhang, X. Liu, B. Zhang, and S. Kumar, "WaveFlex Biosensor: MXene-Immobilized W-shaped Fiber-Based LSPR sensor for highly selective tyramine detection," *Opt. Laser Technol.*, vol. 171, p. 110357, 2024.

[9] R. Singh, S. Kumar, S. Bera, and S. K. Bhunia, "Trends in Using Fluorescent MXene Quantum Dots for Selective Detection and Bioimaging Applications: A Review," *ACS Appl. Nano Mater.*, vol. 6, no. 21, pp. 19526–19550, 2023.

[10] V. S. Chaudhary, D. Kumar, and S. Kumar, "Gold-immobilized photonic crystal fiber-based SPR biosensor for detection of malaria disease in human body," *IEEE Sens. J.*, vol. 21, no. 16, pp. 17800–17807, 2021.

[11] B. Kaur, S. Kumar, and B. K. Kaushik, "MXenes-based fiber-optic SPR sensor for colorectal cancer diagnosis," *IEEE Sens. J.*, vol. 22, no. 7, pp. 6661–6668, 2022.

[12] N. Ayyanar, G. Thavasi Raja, M. Sharma, and D. Sriram Kumar, "Photonic Crystal Fiber-Based Refractive Index Sensor for Early Detection of Cancer," *IEEE Sens. J.*, vol. 18, no. 17, pp. 7093–7099, 2018, doi: 10.1109/JSEN.2018.2854375.

[13] F. Zheng et al., "A Highly Sensitive CRISPR-Empowered Surface Plasmon Resonance Sensor for Diagnosis of Inherited Diseases with Femtomolar-Level Real-Time Quantification," *Adv. Sci.*, vol. 9, no. 14, p. 2105231, 2022, doi: 10.1002/advs.202105231.

[14] K. D. Miller et al., "Brain and other central nervous system tumor statistics, 2021," *CA. Cancer J. Clin.*, vol. 71, no. 5, pp. 381–406, 2021.

[15] "American Brain Tumor Association, Brain Tumor Education." 2021. [Online]. Available: https://www.abta.org/about-brain-tumors/brain-tumoreducation/

[16] "National Brain Tumor Society, Quick Brain Tumor Facts,." 2021. [Online]. Available: https://braintumor.org/brain-tumor-information/braintumor-facts/

[17] "American Society of Clinical Oncology, Cancer Facts & Figures,." 2023. [Online]. Available: https://www.cancer.net/cancer-types/brain-tumor/statistics/

[18] W. M. Nouman, S. E. S. Abd El-Ghany, S. M. Sallam, A. F. B. Dawood, and A. H. Aly, "Biophotonic sensor for rapid detection of brain lesions using 1D photonic crystal," *Opt. Quantum Electron.*, vol. 52, no. 6, p. 287, 2020, doi: 10.1007/s11082-020-02409-2.

[19] T. Wu et al., "Surface plasmon resonance biosensor based on gold-coated side-polished hexagonal structure photonic crystal fiber," *Opt. Express*, vol. 25, no. 17, pp. 20313–20322, 2017.

[20] S. Singh, B. Chaudhary, A. Upadhyay, D. Sharma, N. Ayyanar, and S. A. Taya, "A Review on Various Sensing Prospects of SPR Based Photonic Crystal Fibers," *Photonics Nanostructures-Fundamentals Appl.*, p. 101119, 2023.

[21] V. S. Chaudhary, D. Kumar, and S. Kumar, "Au-TiO 2 coated photonic crystal fiber based SPR refractometric sensor for detection of cancerous cells," *IEEE Trans. Nanobioscience*, 2022.

[22] V. S. Chaudhary, D. Kumar, G. P. Mishra, S. Sharma, and S. Kumar, "Plasmonic biosensor with gold and titanium dioxide immobilized on photonic crystal fiber for blood composition detection," *IEEE Sens. J.*, vol. 22, no. 9, pp. 8474–8481, 2022.

[23] G. R. Berdiyorov, "Optical properties of functionalized Ti3C2T2 (T= F, O, OH) MXene: First-principles calculations," *Aip Adv.*, vol. 6, no. 5, 2016.

[24] D. Pysz et al., "Stack and draw fabrication of soft glass microstructured fiber optics," *Bull. Polish Acad. Sci. Tech. Sci.*, vol. 62, no. 4, pp. 667–682, 2014.

[25] F. Wang, W. Yuan, O. Hansen, and O. Bang, "Selective filling of photonic crystal fibers using focused ion beam milled microchannels," *Opt. Express*, vol. 19, no. 18, pp. 17585–17590, 2011.

[26] R. Zakaria, W. Kam, Y. S. Ong, S. Yusoff, H. Ahmad, and W. S. Mohammed, "Fabrication and simulation studies on D-shaped optical fiber sensor via surface plasmon resonance," *J. Mod. Opt.*, vol. 64, no. 14, pp. 1443–1449, 2017.

[27] Y. Chen et al., "Refractive Index Sensors Based on Ti3C2Tx MXene Fibers," *ACS Appl. Nano Mater.*, vol. 3, no. 1, pp. 303–311, 2020, doi: 10.1021/acsanm.9b01889.

[28] R. Khan and S. Andreescu, "MXenes-Based Bioanalytical Sensors: Design, Characterization, and Applications," 2020.

[29] N. A. Mohammed, O. E. Khedr, E.-S. M. El-Rabaie, and A. A. M. Khalaf, "Brain tumors biomedical sensor with high-quality factor and ultra-compact size based on nanocavity 2D photonic crystal," *Alexandria Eng. J.*, vol. 64, pp. 527–540, 2023.

[30] A. Asuvaran and G. Elatharasan, "Design of two-dimensional photonic crystal-based biosensor for abnormal tissue analysis," *Silicon*, vol. 14, no. 12, pp. 7203–7210, 2022.